Influence of strain rate and Sn in solid solution on the grain refinement and crystalline defect density in severely deformed Cu

Ghenwa Zaher, Ivan Lomakin, Nariman Enikeev, Samuel Jouen, Allisson Saiter, Xavier Sauvage

Influence of strain rate and Sn in solid solution on the grain refinement and crystalline defect density in severely deformed Cu

Ghenwa Zaher[1*], Ivan Lomakin[2,3], Nariman Enikeev[2,4], Samuel Jouen[1], Allisson Saiter-Fourcin[1], Xavier Sauvage[1]

1- Normandie Université, UNIROUEN, INSA Rouen, CNRS, Groupe de Physique des Matériaux, 76000 Rouen, France
2- Laboratory of Mechanics of Advanced Bulk Nanomaterials for Innovative Engineering Applications, Saint Petersburg State University, 198504 Peterhof, Saint Petersburg, Russia
3- Aalto University, Department of Applied Physics, Complex Systems and Materials Group, Espoo, Finland
4- Institute of Physics of Advanced Materials, Ufa State Aviation Technical University, 450008 Ufa, Russia

*Corresponding author: ghenwazaher@gmail.com

Materials Today Communications 26 (2021) 101746
https://doi.org/10.1016/j.mtcomm.2020.101746
Received 23 September 2020; Accepted 1 October

Keywords: Copper alloys; ultrafine-grained structure; severe plastic deformation; crystalline defects

Abstract:

A commercially pure Cu and a Cu-8wt.%Sn alloy were subjected to high pressure torsion (HPT) to study the effect of Sn as solute element and deformation rate on the grain refinement mechanism and the defect accumulation in Cu. The microstructure and hardness of produced ultrafine grained (UFG) states of both materials were carefully characterized. We show that addition of Sn in Cu leads to significant decrease in grain size, accumulation of higher stored energy and increase in hardness accompanied with the delay of hardness saturation with shear strain. Increasing HPT deformation rate induces significant heat dissipation in the processed materials markedly pronounced in CuSn8 as compared to Cu. Surprisingly, deformation rate has the opposite effect on the microhardness of UFG Cu and CuSn8, which decreases with the deformation rate for the case of Cu, while exhibits faster saturation to higher values for CuSn8. We also show that despite higher self-heating at higher deformation rates, higher HPT rotation speed provides reduction in grain size and increase in the defect density for CuSn8 alloy. This effect is assumed to be related to strong interactions between Sn solute atoms and strain-induced defects so that mechanically driven effects prevail over dynamic annihilation of dislocations. Finally, we present a qualitative model based on the phenomena of production and annihilation of dislocations. This model was able to reproduce the evolution of grain size, concentrations defects and hardness with different deformation parameters and after the addition of solute element in material.

1. Introduction

Materials used for electrical contacts require a combination of high electrical conductivity, high oxidation resistance and high mechanical strength for fatigue resistance. Thanks to its high intrinsic electrical conductivity, copper is often selected for such applications, however alloying is usually necessary to adjust mechanical and oxidation properties. Small amounts of Sn, like any other elements, affect the electrical conductivity but is very attractive anyway because it reduces the oxidation kinetics and significantly enhances the mechanical strength thanks to solid solution hardening [1,2]. When environmental conditions do not require specific protection and only mechanical strength matters, alloying can also be used to take advantage of solid solution hardening or precipitate hardening but it will always be at the expense of electrical conductivity [3]. Tuning crystalline defect densities is another interesting strategy and it has been shown for example that a high density of nanotwins in pure Cu may give rise to a yield stress up to 1 GPa with an electrical conductivity close to 95% of International Annealed Copper Standard (IACS) [4]. Following the well-known Hall Petch law [5], grain refinement is also attractive. It has been demonstrated that UFG structures could relatively easily be obtained in metallic alloys thanks to Severe Plastic Deformation (SPD) methods [6–8]. Grain refinement mechanisms during SPD are controlled by the dynamic reorganization of crystalline defects that are continuously created and annihilated. After a critical value of plastic strain, a saturation of the hardness is often reported. It corresponds to a saturation regime where a balance between the creation and the annihilation of crystalline defects is reached [9]. The critical value of plastic strain necessary to reach this saturation and the corresponding grain size depend on the applied strain [10], the temperature [11–13], the strain rate [14–17] and alloying elements [18–23]. For commercially pure Cu, the typical grain size stands in a range of 150 to 400 nm with a micro-hardness of 130 to 180 HV [24–27]. It has been shown experimentally that further grain refinement can be achieved at high strain rate or low temperature to reduce defect recovery or to generate a high density of twins [11] [14]. Solute elements that significantly interact with dislocations also usually lead to much smaller grain sizes, down to only 20 nm in some specific cases [28].
In the present work, we have systematically investigated the combined influence of solute elements and strain rate on the grain size refinement and crystalline defect densities of copper subjected to SPD. Sn has been selected as alloying element regarding potential applications for electrical contacts where high mechanical strength is required together with a good oxidation resistance. A simple model based on the production and annihilation of defects is also proposed for a better understanding of the revealed relationships between processing parameters (including alloy composition) and resulting UFG structures.

2. Experimental materials and procedures

Two commercial materials were used for the experimental work carried out for this study: pure copper (99.9%) and a CuSn8 alloy containing 8 wt.% of Sn. The delivered extruded bars (20 mm diameter) were annealed at 700°C during 1h under vacuum for complete recrystallization and solid solution treatment of the CuSn8 alloy. Discs (20 mm diameter) were then sliced and severely deformed by HPT processing at room temperature, under a pressure of 6 GPa. HPT strain levels reported in the following correspond to the shear strain estimated from $\gamma = 2 \pi r N / t$ where N is the number of revolutions, t the sample thickness and r the distance from the torsion axis. To investigate the influence of the strain rate, two different strategies have been explored, first by changing the rotation speed (0.5, 1 and 2 rotations per minute (rpm)) and second by changing the HPT-disc thickness (1 and 2 mm). To

monitor sample temperature increase during the HPT process, a pyrometer « Optris CTlaser 3M » was used. The infrared spot was focused on the upper anvil at the closest location near the sample. Only temperatures higher than 150°C could be measured with this setup, thus data could not be recorded for all deformation conditions.

Mechanical properties were evaluated by microhardness measurements performed at room temperature using a Future tech FM7 device with a diamond pyramid indenter, a load of 500g and a dwell time of 15 s. Microhardness values were measured across the diameter of HPT disks with spatial steps of 0.5 mm. Data provided in the following are the average of at least 10 measurements.

The thermal stability and the stored energy were evaluated thanks to differential scanning calorimetry (DSC). Measurements were carried out under a purified nitrogen atmosphere in a Q100 DSC apparatus with heating rates ranging from 2.5 to 40°C/min. Two DSC runs were performed on each sample to check that the recyclization was completed during the first run, and to use the second as a baseline. Samples of 8 to 12 mg were cut at the periphery of HPT discs where the microhardness was usually found relatively uniform (outer region between the edge and 8 mm from the centre). The stored energies of samples deformed by HPT were estimated from the area of the exothermic peak resulting from recrystallisation. The apparent activation energy for recrystallization E was estimated based on the Kissinger method and using the following equation and a linear interpolation [29]:

$$\ln\left(\frac{\alpha}{T_P^2}\right) = -\frac{E}{RT_P} + C \qquad (1)$$

Where α is the heating rate, T_P is the temperature of the exothermic peak, C a constant and R the gas constant (8.314 J mol^{-1} K^{-1}). Recrystallization temperatures were also estimated based on this linear interpolation for a virtually null heating rate.

Microstructures were characterized by Transmission Electron Microscopy (TEM) using a JEOL ARM-200F microscope operated at 200 kV. Scanning TEM (STEM) imaging was performed with a probe size of 0.2 nm and dark field images were recorded with collection angles ranging from 20 to 80 mrad. TEM samples were prepared in different regions of HPT discs and electron transparency was achieved by jet polishing in a solution of 30% nitric acid and 70% methanol under a voltage of 12 kV at a temperature of -30°C. The microstructure was analyzed on the top view of HPT disc. Structure analysis was also carried out by X-Ray diffraction using a Bruker D8 diffractometer in Bragg-Brentano geometry (CoKα radiation) with a step size of 0.02° and a collection time of 2 seconds per point. X-ray diffraction analysis was performed by the refinement of full X-ray profile (Rietveld method) realized in the Maud software [30]. Instrumental broadening was removed by the treatment of data collected for the Al_2O_3 standard sample under the same measuring conditions.

3. Results

3.1 Influence of Sn in solid solution on micro-hardness and on the UFG structure resulting from SPD

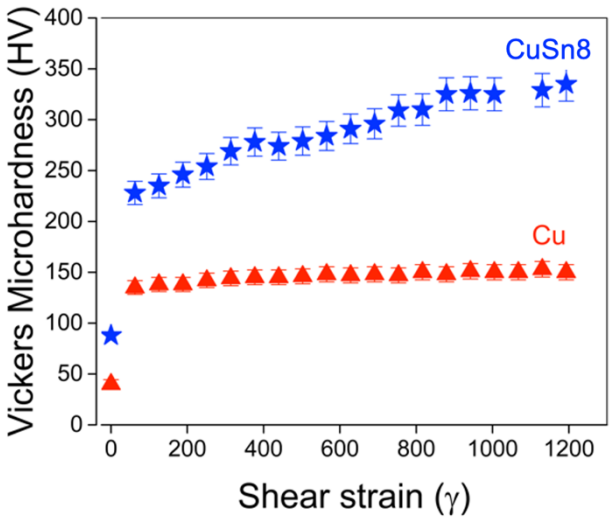

Figure 1: Vickers micro-hardness of Cu and CuSn8 alloy as a function of the shear strain applied by HPT (1mm samples, 1 rpm).

The Vickers micro-hardness of Cu and CuSn8 alloy have been measured along the HPT discs diameters and plotted in Fig. 1 as a function of the shear strain. As compared to the initial hardness of annealed materials (40±2 and 88±5 HV for Cu and CuSn8 respectively), a significant hardening occurred, as expected. The microhardness of Cu is relatively constant with only a small gradient and a maximum value of 150 ± 10 HV that is reached at about $\gamma \approx 200$ where saturation starts in agreement with earlier studies [31,32]. The microhardness saturation of CuSn8 occurs at a much larger shear strain ($\gamma \approx 800$) and at a much higher level than Cu (up to 330 ± 20 HV). Part of this difference is the well-known solid solution hardening effect which results from the interaction between solutes and dislocations giving rise to a higher hardness in the annealed state ($\Delta HV \approx 50$). However, after SPD, the hardness difference becomes much higher ($\Delta HV \approx 180$), indicating some significant difference in microstructure and crystalline defect densities. TEM observations were carried out to clarify this point (Figs. 2a and 2b) and as shown on distributions (Figs. 2c and 2d), both the grain size distribution and the mean grain size is much larger in Cu than in CuSn8 (380±150 nm against 130±60 nm respectively) in the HV saturation regime ($800<\gamma<1200$). This large difference is in relatively good agreement with earlier studies on the Cu-Sn system [23]. Additionally, some twins were often observed inside grains of the CuSn8 alloy processed by HPT (arrowed in Fig. 2b) but never in Cu. It has been shown that intensive twinning might occur in pure copper deformed at high strain rate [33,34]. In the present study however, much lower strain rates were applied, and twinning is simply connected to Sn that lowers the stacking fault energy of copper [23].

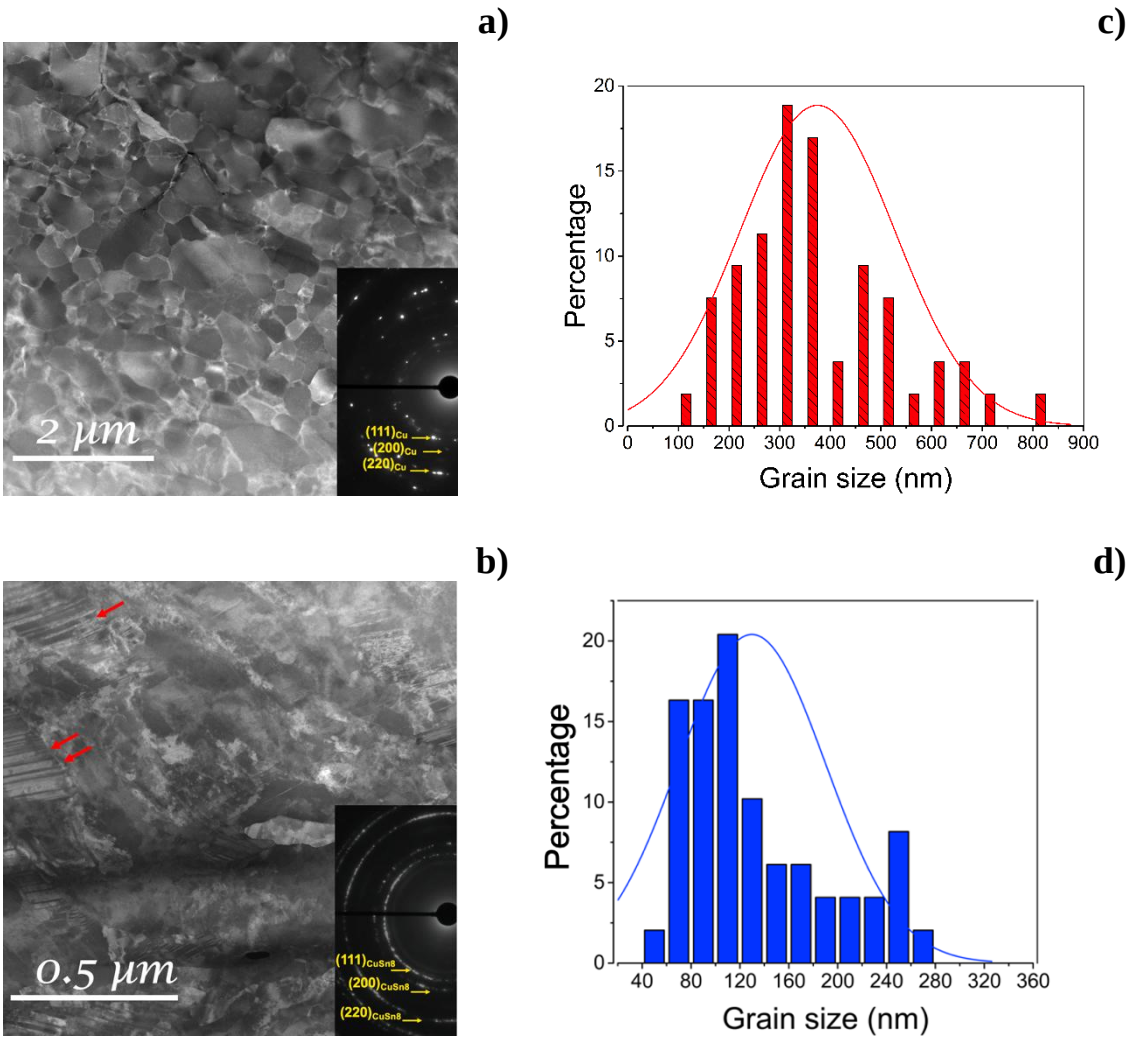

Figure 2: Dark field STEM images of Cu (a) and CuSn8 (b) processed by HPT (800<γ<1200, 1mm samples, 1 rpm) with corresponding SAED patterns (insets) Arrows in b) point twins resulting from SPD. Corresponding grain size distributions (c) and (d) were estimated from these images.

DSC was used to evaluate the amount of stored energy in UFG structures. Measurements were performed at various heating rates (5, 10, 20 and 30 °C/min), and as expected an exothermic peak was always detected (Fig. 3). This peak is shifted to higher temperatures at higher heating rates which is fully consistent with the recrystallization process.

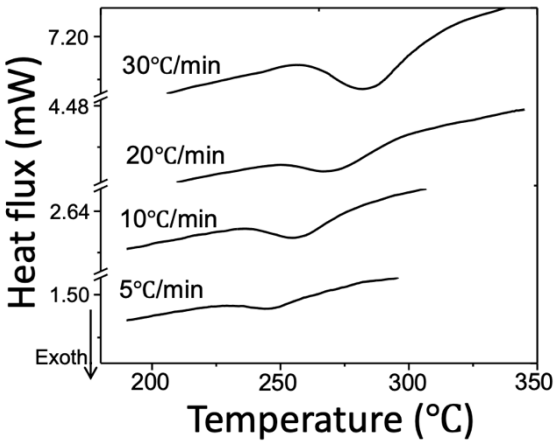

Figure 3: DSC thermograms at different heating rates of Cu processed by HPT (1mm samples, 1 rpm).

Recrystallization temperatures, activation energies and stored energies estimated from DSC measurements carried out on Cu and CuSn8 processed by HPT are listed in table 1. Data corresponding to Cu are fully consistent with literature data [25,35–37] and are systematically lower than those corresponding to CuSn8. Thus, the addition of Sn to Cu increases the recrystallization temperature by 100°C, the activation energy by a factor of 2 and the stored energy by a factor of 3. The much higher stored energy is fully consistent with hardness measurements and TEM observations that indicate a higher defect density and a smaller grain size. Then, the driving force for recrystallization (linked to the stored energy) being much higher in CuSn8 than in Cu, a lower recrystallization temperature might have been expected but it is absolutely not the case. This is a clear indication of very strong interactions between Sn solute atoms and crystalline defects (especially dislocations and GBs) that delay the recrystallization kinetics.

Material	**T_R (°C)**	**Activation energy (kJ.mol^{-1})**	**Released energy (J.g^{-1})**
Cu	227±7	92±6	0.97±0.12
CuSn8	327±3	200±30	3.2±0.3

*Table 1: Recrystallization temperatures, activation energy and stored energy estimated from DSC measurements for Cu and **CuSn8** processed to HPT (1mm samples, 1 rpm).*

.

3.2 Influence of the strain rate on the UFG structure resulting from SPD

Since UFG structures achieved by SPD result from the dynamic reorganization of crystalline defects, not only solutes but also the strain rate should have an influence. This parameter could be manipulated whether by changing the HPT disc thickness or by changing the rotation speed.

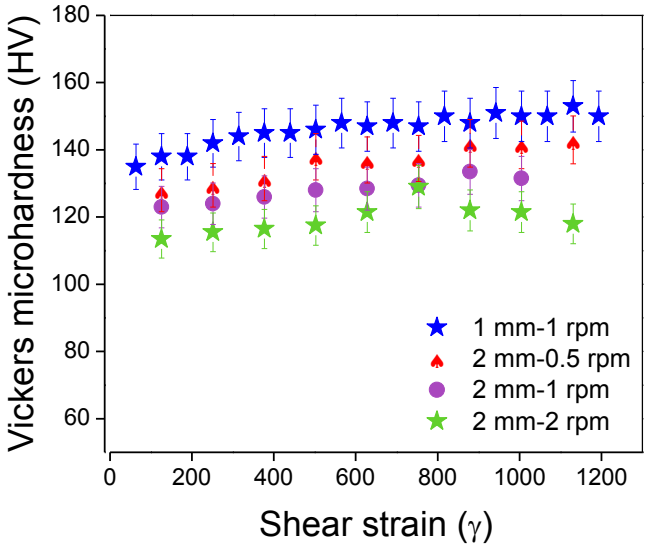

Figure 4: Micro-hardness as a function of the shear strain for Cu processed by HPT at various rotation speeds (2mm samples) and compared to the 1mm sample processed at 1rpm.

The micro-hardness of 2 mm thick Cu samples processed by HPT is plotted as a function of the rotation speed in Fig. 4. A significant influence of the rotation speed is exhibited: the highest it is, the lowest the micro-hardness. There is a softening of about $\Delta HV \approx 20$ at 2 rpm as compared to 0.5 rpm with micro-hardness saturation values of 142±7 HV and 122±6 HV respectively. Surprisingly, the 1mm thick sample exhibits a significantly higher hardness ($\Delta HV \approx 25$) as compared to the 2mm thick sample deformed at a similar strain rate (2 rpm).The heat generated by the plastic work during HPT is dissipated into anvils and thanks to their high thermal conductivity, the temperature increase is usually relatively limited [38]. However, the produced amount of heat is proportional to the volume of the deformed samples and thus higher for thicker samples. Then, a higher temperature was most probably reached in thicker samples, leading to a higher rate of crystalline defect recovery and thus a significant softening as compared to the thinner samples.

The influence of the shear strain on the micro-hardness of CuSn8 is displayed on Fig. 5 where the influence of the rotation speed is shown for the 2mm thick samples. There is no shear strain range with a saturation of the micro-hardness at 0.5 rpm, while saturation is observed for $\gamma > 900$ and $\gamma > 100$ at 1 rpm and 2 rpm respectively. Besides, whatever the rotation speed, the maximum micro-hardness value is similar (380 ± 20 HV). Thus, it seems that saturation is reached at lower shear strain when the strain rate is higher and contrary to Cu there is no significant softening.

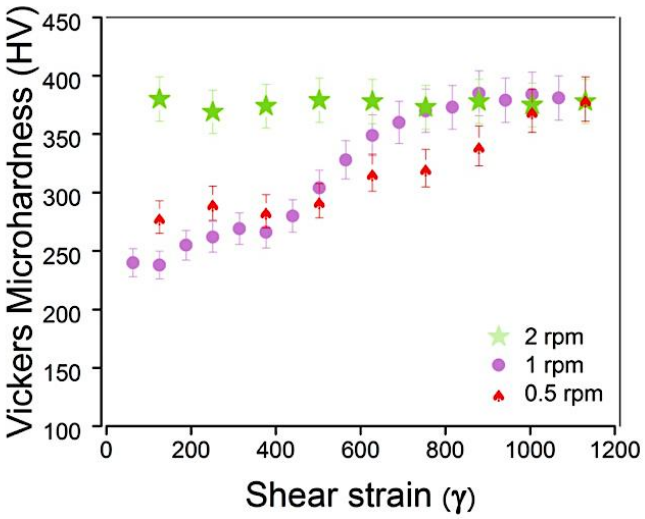

Figure 5: Micro-hardness as a function of the shear strain for CuSn8 processed by HPT at various rotation speeds (2mm samples).

Due to the high thermal conductivity of anvils, the temperature increase during deformation is relatively for metallic alloys with low yield stresses at low rotation speeds [38], and this is why at rotation speeds of 0.5 and 1 rpm it was impossible to detect any significant temperature increase of anvils during deformation of Cu or CuSn8 (1 and 2 mm thick samples). However, as shown on Fig. 6, at a rotation speed of 2 rpm, the temperature of anvils reached progressively temperatures higher than 150°C (minimum sensitivity of the experimental setup). It seems to saturate at about 180°C for Cu, while it continuously increases up to about 240°C for CuSn8 at 40 revolutions. The yield stress of CuSn8 being much higher than Cu, it logically leads to more plastic work and heat. Then, if the softening of Cu processed by HPT at the highest rotation speed (Fig. 4) can be attributed to more pronounced dynamic recovery of defects due to the highest temperature, it is apparently not the case for CuSn8 (Fig. 5). It should be noted however that the temperature reached during HPT is closer to the recrystallization temperature for Cu than for CuSn8 (see table 1, (ΔT ~ 60°C and ~90°C respectively), thus a higher mobility of defects is expected.

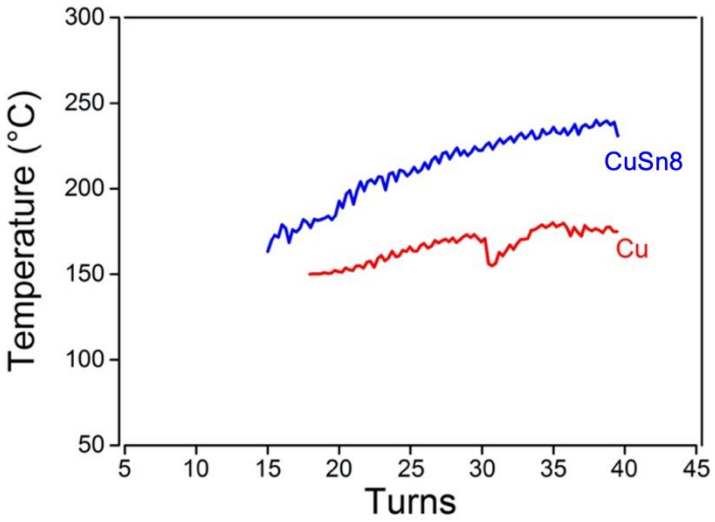

Figure 6: Local temperature rise against time during HPT processing of Cu and CuSn8 at strain rate of 2 rpm. Temperatures below 150°C could not be recorded (2mm samples).

But, for the CuSn8 alloy, the situation is more complex because of Sn solid solution that significantly affects the mobility of dislocations and also because this solid solution is metastable at room temperature [39]. During deformation, the high density of defects may promote atomic mobility and phase separation [40,41], and thus the precipitation of the Cu_3Sn phase. X-Ray diffraction measurements were carried out (Fig.7) but diffraction patterns do not exhibit any peak that could be attributed to the stable Cu_3Sn phase or any significant shift of fcc Cu peaks as compared to the undeformed material, indicating that Sn remained in solid solution. There is however a more pronounced peak broadening at 2 rpm as compared to 1 rpm (Fig. 7b). The corresponding microstrains (at γ~380) were evaluated and they are $4.7 \times 10^{-3} \pm 0.2 \times 10^{-3}$ and $2.3 \times 10^{-3} \pm 0.21 \times 10^{-3}$ respectively. Since these microstrains are mainly related to lattice defect concentrations, it indicates that at 2 rpm the average lattice defect concentration is much higher which is consistent with microhardness measurements (Fig. 5).

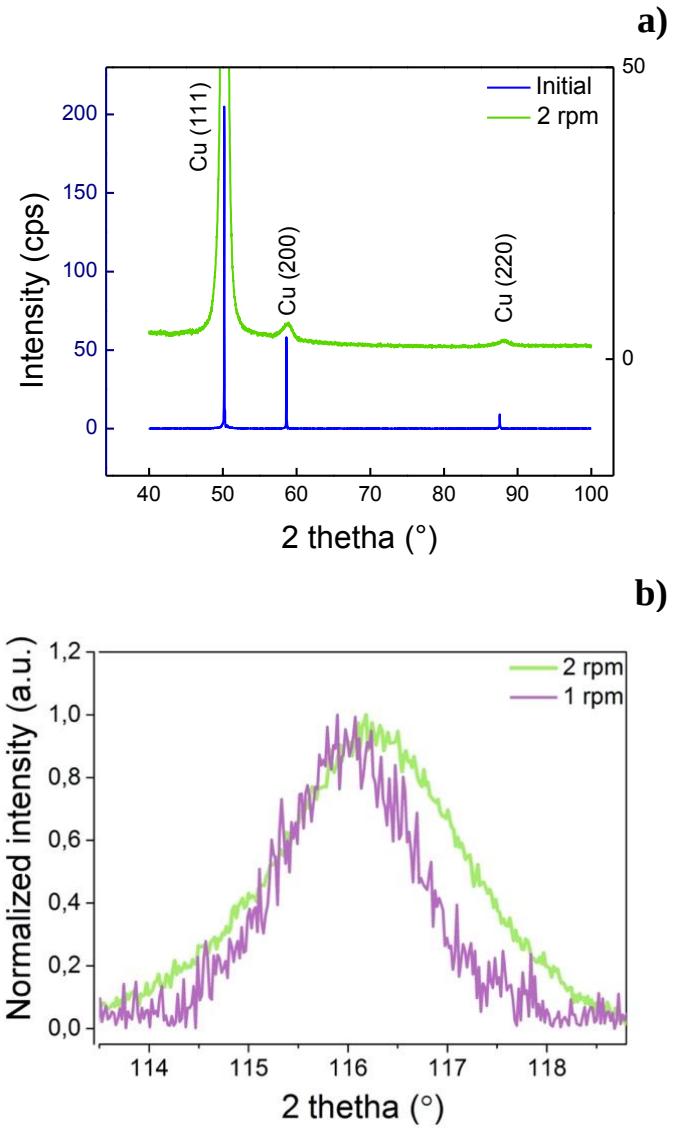

Figure 7: (a) comparison of X-ray diffraction patterns of CuSn8 in the initial state (blue) and after HPT processing at 2 rpm (green) ; (b) (222)Cu peak of CuSn8 after HPT at 1 rpm (purple) and 2 rpm (green), 2mm samples.

Microstructures of the CuSn8 alloy processed by HPT were carefully examined by TEM for a true strain of γ = 380 and rotation speeds of 1 and 2 rpm. Although the microhardness is significantly different for these two states (270±15 and 370±20 HV respectively, Fig. 5), microstructures look relatively similar (Figs. 8a and 8b), with ultrafine grains and large densities of crystalline defects. However, the grain size distributions that were estimated from dark field TEM images clearly show that a significantly finer structure is obtained at higher strain rate (Fig. 8c). Besides, HAADF-STEM imaging did not reveal any Cu_3Sn particles, or Sn segregations along crystalline defects in both states, confirming that Sn was kept in solid solution during deformation as demonstrated by XRD.

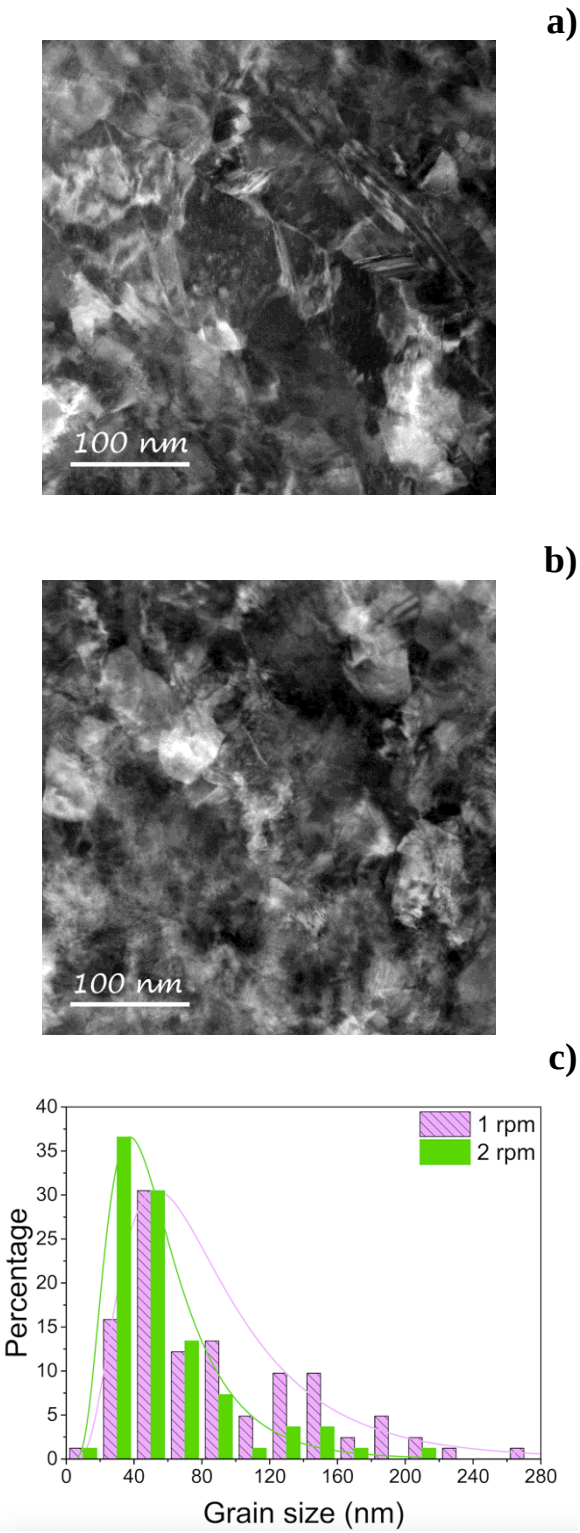

Figure 8: Dark field TEM micrographs of UFG CuSn8 processed by HPT (γ = 380) at 1 rpm (a) and 2 rpm (b), and corresponding grain size distributions (c), 2mm samples.

4. Discussion

4.1 Crystalline defects densities and relationship with mechanical behavior

The addition of Sn in solid solution in Cu has a significant influence on the microstructure evolution during HPT and on the resulting micro-hardness. It leads indeed to a much smaller grain size (130±80 nm against 380±150 nm, Fig. 2) and a higher density of crystalline defects resulting in a significantly higher stored energy (0.97±0.12 and 3.2±0.3 $J.g^{-1}$ respectively, see table 1). The solid solution of Sn in copper also shifts to higher plastic strain the saturation of micro-hardness. Solute-defect interactions are most probably the main reason for this difference as they affect the mobility of crystalline defects leading to delayed recovery and recrystallisation mechanisms [22]. After processing, these interactions also affect the thermal stability and significantly delay the static recrystallization of the UFG CuSn8 (table 1) even if the stored energy (and thus the driving force for recrystallisation) is much higher than in pure copper.

The influence of the strain rate during HPT of pure copper has a relatively small influence. At a rotation speed of 2 rpm, the heat generated by the plastic work leads to a temperature increase due to insufficient heat flow through anvils (Fig. 6). This gives rise to more defect recovery during the process and softening (140±10 against 120±10 HV at saturation for 0.5 rpm and 2 rpm respectively, see Fig. 4). For CuSn8, the dissipated heat and the temperature reached is higher (Fig. 6) but surprisingly the strain rate does not affect the micro-hardness measured at saturation (within the amplitude investigated, see Fig. 5). It has however a remarkable influence on the critical strain required to reach this saturation (γ=1200, 800 and 100 for 0.5, 1 and 2 rpm respectively). This feature points out the complexity of the physical processes that operate during severe plastic deformation where defects are continuously created and annihilated at various rates depending on solute/defects interactions and temperature.

The quantification of defects can hardly be done exclusively using microscopy techniques like TEM. For example, dislocation densities are difficult to measure in severely deformed structures, but the combination with DSC data could help to clarify this point. If the elastic energy due to internal stresses is neglected, then the total stored energy during deformation *E* is connected to crystalline defects and may be written as:

$$E = E_{GB} + E_{twins} + E_{vac} + E_{dis} \qquad (2)$$

Where E_{GB} is the energy of GBs, E_{twins} is the energy of twins, E_{vac} is the energy of vacancies and E_{dis} is the energy of dislocations.

It is well known that the vacancy concentration in metallic alloys processed by SPD could be much higher than equilibrium concentrations and values up to 10^{-5} have been reported [42–44]. Considering the formation energy of a vacancy in copper ($1.57\times 10^{-19} J$ [45]), such concentration gives an upper estimate of $E_{vac} < 0.02$ $J.g^{-1}$. This is only few percent of the stored energy measured by DSC (table 1), thus these defects could be neglected in equation *(2)*.

The GB stored energy per unit volume can be described as:

$$E_{GB} = \frac{6}{d}\gamma_{GB} \qquad (3)$$

Where d is the mean diameter of grains (assumed spherical) and γ_{GB} is the GB energy of copper ($\gamma_{GB} = 0.625\ J.m^{-2}$ [46]). Thus, the mean contribution of grain boundaries is about 0.56 and 1.60 $J.g^{-1}$ for Cu and CuSn8 respectively (saturation regime, HPT at 1 rpm), which is about half of the total stored energies measured by DSC measurments (table 1).

For CuSn8, relatively large twin densities could be observed by TEM (Fig. 2b) and they contribute to the remaining stored energy. The energy per unit volume associated to twin boundaries writes as:

$$E_{twins} = A_t \gamma_t \quad (4)$$

Where A_t is the surface area of twins per unit volume and γ_t is the twin boundary energy (taken as the stacking fault energy, $\gamma_{t\,(CuSn)} = 0.035\ \mathrm{J}.m^{-2}$ [47]). The mean distance between twins was estimated from TEM images (20±10 nm for CuSn8 processed hy HPT at 1 rpm) and A_t was estimated as $A_t = 1 / d_{twins}$. It yields to an additional stored energy of about 0.20 $J.g^{-1}$ for CuSn8.

Last, assuming that dislocations are homogeneously distributed, the stored energy associated to their stress field can be written as [48]:

$$E_{dis} = \left(AGb^2 \frac{N}{4\pi} ln(\frac{1}{b\sqrt{N}}) \right) / \rho \quad (5)$$

Where N is the dislocation density (m^{-2}), G is the shear modulus (G= 46 GPa for Cu [49]), b is the magnitude of the Burgers vector (b = 2.56x10^{-10} m for (110) dislocations in fcc Cu [50]) and A is a constant depending on dislocations type (A =1 for screw dislocations).

Then, equations *(2, 3, 4 and 5)* give E_{dis} = 0.41 and 1.40 $J.g^{-1}$ in Cu and CuSn8 (after HPT at 1 rpm in the saturation regime), corresponding to dislocation densities of about 10^{15} and 10^{16} m^{-2} respectively. These values are consistent with literature data for pure Cu [51] and clearly demonstrate that the crystalline defect density is much higher in CuSn8 than in Cu. This is most probably due to the influence of solutes Sn atoms that strongly interact with defects and reduce dynamic recovery processes. All these defects (GBs and dislocations) contribute to the micro-hardness *HV*, and the above estimates clearly explain why the hardness difference beteween Cu and CuSn8 at saturation (ΔHV ≈ 250, see Fig. 1), is much higher than the solid solution hardening measured in the coarse-grained state (ΔHV ≈ 50).

Thus, Sn in solid solution stabilizes more defects but when the strain rate is increased, a smaller grain size is achieved within a shorter time (60 and 90 nm at γ = 380 for $\dot{\gamma} = 0.628$ and $0.314\ s^{-1}$ respectively, see Fig. 8). Assuming that the total amount of defects that was created during the plastic deformation was the same (in other words, assuming that it is simply proportional to the total strain), then the smaller grain size measured at higher strain rate could be only the result of: i) a faster reorganization of defects leading to more boundaries; or ii) a smaller number of defects annihilated during the process. XRD data show that much higher micro-strains exist in the material processed at higher strain rate (Fig. 7), which is consistent with the second hypothesis. So, even if the temperature is significantly higher, Sn atoms still significantly reduce the mobility of crystalline defects at higher strain rate.

The mobility of boundaries is also an important parameter and in Mg alloys, the smaller grain size achieved at higher strain rate during SPD has been attributed to a reduced grain growth during dynamic recrystallization [17,52]. It is however apparently more critical in Mg deformed near room temperature, i.e. at a much lower homologous temperature than in Cu.

4.2 Theoretical approach

During SPD, grain size refinement results from defects generation and their annihilation or reorganization. Our experimental data demonstrate that these phenomena are significantly affected by the presence of solute atoms (Sn) and the strain rate. To confirm that the key parameter is the reduced mobility of defects due to solute/defect interactions, we propose to

apply a simple dislocation based model adapted from the approach initially proposed by Kocks-Mecking [53]. The microstructure evolutions during severe plastic deformation will be treated through the evolution of the dislocation density in order to predict qualitatively the influence of temperature, plastic strain, strain rate and solute atom concentration. For the sake of simplicity, we will assume that the grain refinement results mainly from dislocation activity (twins and vacancies will be neglected). Dynamic recrystallization and grain boundary motions will not be considered neither, therefore we just aim at a qualitative approach.

The evolution of the dislocation density results from a balance between generated and annihilated dislocations. In a first step, if only annihilation with other dislocations or at grain boundaries are considered, the time evolution of the dislocation concentration C can be written as:

$$\frac{dC}{dt} = A_1\dot{\gamma} - A_2 C - A_3 \frac{C}{d} \qquad (6)$$

The first term is the dislocation production rate, $\dot{\gamma}$ being the deformation rate and A_1 a positive constant. The second term is associated with the annihilation of dislocation with other dislocations. It is proportional to the dislocation concentration C and A_2 is a positive constant which reflects the dislocation mobility. Thus, A_2 will be a function of solute concentration and temperature. The third term governs the rate of dislocation annihilation at grain boundaries. It is proportional to the surface to volume ratio of grains (for spherical grains ~ 1 / d with d the mean grain size) and A_3 is a positive constant that reflects the dislocation mobility and absorption rate at boundaries. Thus, A_3 is also a function of the solute concentration and temperature.

There is an initial grain size d_0 corresponding to an initial surface of grain boundary per unit volume S_0 (for spherical grains, $S_0 \sim 1 / d_0$). During deformation, new boundaries are also created by accumulation of dislocations, leading to an additional surface of grain boundary per unit volume S_c. Then, the new grain size d writes as:

$$\frac{1}{d} = S_0 + S_c = \frac{1}{d_0} + S_c \qquad (7)$$

Assuming that the growth rate of S_c is simply proportional to the dislocation concentration, then:

$$\frac{d}{dt}S_c = A_4 \frac{dC}{dt} \qquad (8)$$

Thus,

$$\frac{1}{d} = \frac{1}{d_0} + \int_0^t A_4 \frac{dC}{dt} dt \qquad (9)$$

The combination of Eq. *(6)* and *(9)* cannot be solved analytically, therefore a step integration of Eq. (6) was carried out as follow:

$$C_n = C_{n-1} + \Delta t(A_1\dot{\gamma} - A_2 C_{n-1} - A_3 \frac{C_{n-1}}{d_{n-1}}) \qquad (10)$$

Where C_i and d_i are the dislocation density and the grain size at the i^{th} step and Δt is the time increment between two steps.

After each step, the new grain size was calculated from Eq. (*9*) as follow:

$$d_n = \frac{1}{\frac{1}{d_{n-1}} + A_4 C_n} \qquad (11)$$

Arbitrary values were given to the four constants A_1, A_2, A_3 and A_4 but they have been adjusted with the following physical criteria: i) annihilation could not be stronger than creation; ii) dislocation density C has to evolve within several orders of magnitude; iii) grain size has to decrease by more than two orders of magnitude. For the sake of simplicity, C_0 was set to zero. Primary results are displayed on Fig. 9 where it clearly appears that the dislocation density increases sharply in the early stage of deformation, it reaches a maximum and then decreases to progressively stabilize (Fig. 9a). This is obviously connected with the grain size reduction (Fig. 9b) and thus the creation of new interfaces that annihilate dislocations. A higher strain rate leads to a higher dislocation density (Fig. 9a) but has only a very small influence on the grain size (less than 1% in Fig. 9b). This is connected to a higher production rate (proportional to the strain rate) that is not balanced by a significantly higher annihilation rate (same *A2*, *A3* and *A4* constants in Eqs. (*10*) and (*11*)).

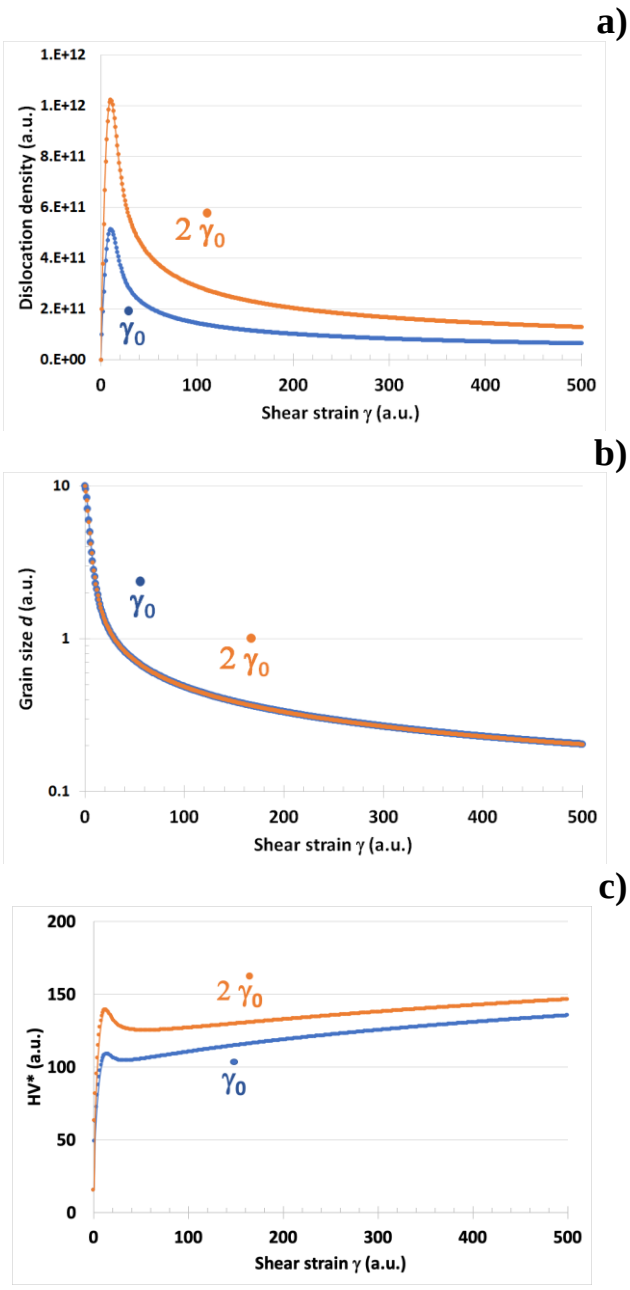

Figure 9: Qualitative evolution of the dislocation density (a), of the grain size (b) and of the micro-hardness (c) as a function of the shear strain, as estimated from Eqs. (10), (11) and (12). Calculations were carried out for two different strain rates ($\dot{\gamma}_0$and $2\dot{\gamma}_0$). All units are arbitrary.

In the experimental study, only the micro-hardness evolution was systematically measured as a function of the shear strain, therefore it is necessary then to link these microstructure evolutions to the micro-hardness. The output of the model is in arbitrary units, but relationships with the dislocation density and the grain size are known (Bailey-Hirsch and Hall-Petch law respectively [31, 32, 50]) and the corresponding hardness *HV** may be approximated as follow:

$$HV^* = HV_0^* + \frac{A_5}{\sqrt{d}} + A_6\sqrt{C} \qquad (12)$$

Where HV_0^* is the initial microhardness (including also the solid solution hardening) and A_5 and A_6 are positive constants. To have a relatively physical representation of the micro-hardness evolution, A_5 and A_6 constants were selected with the following criteria: i) the hardness should increase by a factor of about 10 within the range of shear strain; ii) the maximum contribution of dislocations (for the maximum dislocation density) should be nearly half of the maximum contribution of grain boundaries (for the minimum grain size).

Fig. 9c shows the evolution of the micro-hardness estimated from Eq. *(12)* corresponding to the dislocation density and the grain size evolution of Fig. 9a and 9b. The trend is in relatively good agreement with our experimental data for Cu (Fig. 1), with a sharp increase in the early stage of deformation and then a plateau. One can notice however a small overshoot at the transition between the two regimes corresponding to the maximum of dislocation density. This small difference is probably due to the limit of the Bailey-Hirsch type relationship taken in Eq. (12) and that is no more valid for very large dislocation densities (where dislocations are necessarily not homogeneously distributed anymore). It is also important to note the relatively small but constant slope at large deformations while our experiments, like others from literature, exhibit a saturation regime. This difference is attributed to the boundary mobility during SPD [54,55] that was neglected in our model and that should limit the grain size reduction.

Micro-hardness curves plotted for different strain rates (Fig. 9c) show that it is significantly higher at higher strain rate which is naturally linked to the highest calculated dislocation density (since the grain size contribution is very close). This trend is not in agreement with our experimental data for Cu (Fig. 4), confirming that at higher strain rates, the mobility of defects and thus their ability to annihilate is enhanced. This is most probably due to a temperature increase which is not considered in Eq. *(6)*.

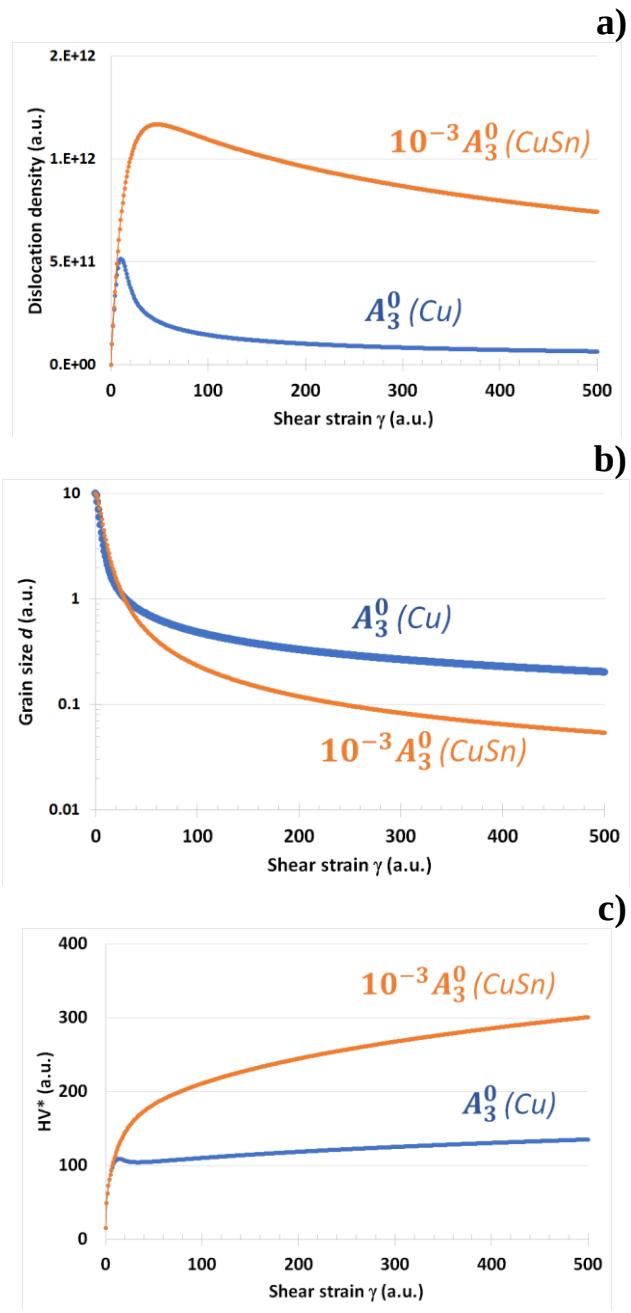

Figure 10: Qualitative evolution of the dislocation density (a), of the grain size (b) and of the micro-hardness (c) as a function of the shear strain, as estimated from Eqs. (10), (11) and (12). Calculations were carried out for two different values of the A_3 constant that accounts for the annihilation of dislocations at boundaries. It is connected to the dislocation mobility which is lower in CuSn8 due to Sn in solid solution and A_3^0 refers to the constant taken as reference for Cu. All units are arbitrary.

The addition of Sn in solid solution might affect constants in equations *(6)* and *(7)*. However, if it is considered that: i) the dislocation production rate is mainly controlled by the strain rate; ii) the annihilation of dislocations with other dislocations is intrinsically random and its amplitude mainly related to the dislocation density; iii) the number of dislocations required to create new boundaries is just related to defect structure and crystalline lattice. Then, *A1*, *A2* and *A4* respectively should not be significantly affected by Sn in solid solution contrary to *A3* that accounts for the annihilation of dislocations at boundaries. It is indeed connected to the

dislocation mobility and solute atoms will strongly reduce this parameter. The influence of this parameter is presented in Fig. 10. A lower value of A_3 clearly leads to a much higher dislocation density during straining and a significantly smaller grain size. This is fully consistent with our TEM observations showing a smaller grain size in CuSn8 than in Cu (Fig. 2) and with our DSC measurements that revealed a much higher stored energy (table1) and especially one order of magnitude difference in dislocation densities (see previous subsection). The resulting micro-hardness is naturally much higher, also consistent with our experimental data (Fig. 1). Since the boundary mobility was neglected in Eqs. *(6)* and *(7)*, again curves do not exhibit saturation like in Fig. 9.

When the annihilation of dislocations at boundaries is reduced because of a lower mobility of dislocations (CuSn8), a higher strain rate leads to a higher dislocation density (Fig. 11a) like in Cu (Fig. 9a). However, the grain size difference becomes now significant and a higher strain rate gives rise to a smaller grain size (Fig. 11b) which is fully consistent with our TEM data on CuSn8 (Fig. 8). These microstructural differences give rise to a fastest increase of the micro-hardness in the early stage of deformation and to a higher end-value at higher strain rate (Fig. 11c) but the model does not really reproduce the delayed hardness saturation observed experimentally at lower strain rates (Fig. 5). This difference is attributed to the relatively simple approach behind the main equations used here and especially the mobility of boundary that was not taken into account [54,55].

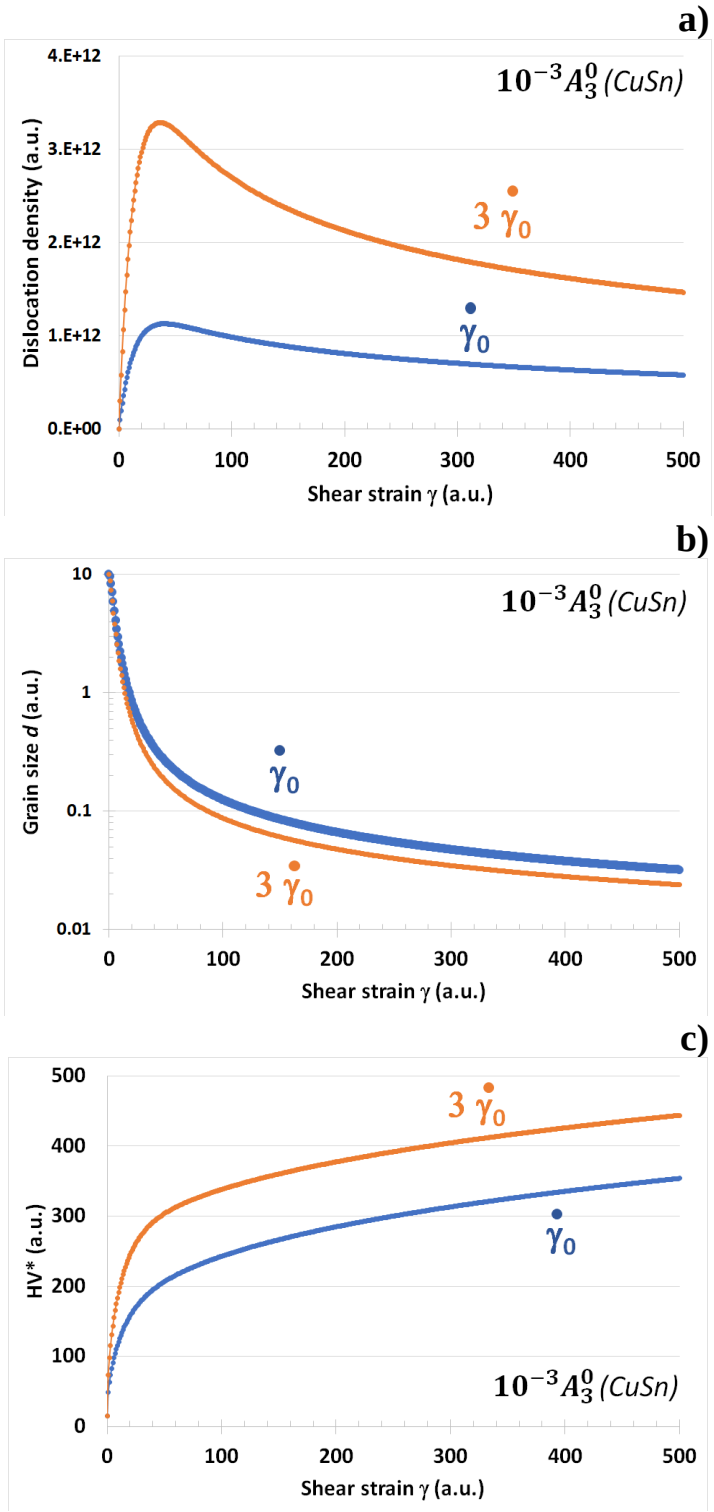

Figure 11: Qualitative evolution of the dislocation density (a), of the grain size (b) and of the micro-hardness (c) as a function of the shear strain, as estimated from Eqs. (10), (11) and (12). Calculations were carried out for two different strain rates using and considering a dislocation annihilation rate at boundaries much lower than in Fig. 9 to account for the effect of Sn in solid solution. All units are arbitrary.

5. Conclusions

(i) Sn in solid solution leads to significantly enhanced grain refinement in Cu subjected to HPT. The grain size of the produced UFG Cu in the steady state is reduced down to 380 nm, while adding 8 wt.% of Sn promotes reducing of the grain size down to 40-60 nm. The saturation of microhardness of CuSn8 is achieved at a much larger shear strain ($\gamma \approx 800$ vs $\gamma \approx 100$) and at a much higher level than Cu (up to 330 HV vs 150 HV, respectively).
(ii) The addition of Sn to Cu provides accumulation of much higher stored energy in the UFG alloy: the recrystallization temperature is increased by 100°C, the activation energy – by a factor of 2 and the stored energy – by a factor of 3.
(iii) Increasing HPT deformation rate induces significant heat dissipation in the processed material. Noticeable strain-induced temperature rise is observed for the rotation speed of 2 rpm being higher for CuSn8 (progressively growing up to 240°C) than for Cu (saturated at 180°C).
(iv) Increasing deformation rate has the opposite effect on the microhardness of UFG Cu and CuSn8. Hardness of Cu decreases with growing the deformation rate, while faster saturation of hardness values is observed for CuSn8 with increasing deformation rate.
(v) Grain size is reduced and the defect density is increased for CuSn8 alloy processed at higher deformation rate despite higher self-heating. This effect is due to strong interactions between Sn solute atoms and crystalline defects that delay the recrystallization kinetics, so that the grain refinement and defect accumulation are mostly mechanically driven in CuSn8.
(vi) The qualitative model based on the phenomena of production and annihilation of dislocations during HPT is able to predict the effect of deformation parameters and solute elements on the evolution of defects concentration, grain size and hardness of deformed materials.

6. Acknowlegements

NE acknowledges the support by Saint Petersburg State University via Lot-2017 Applied (id: 26130576).

7. Data availability

The raw and processed data required to reproduce these findings are available on request to the corresponding author.

References

[1] M.N. Dubey, S. Jouen, X. Sauvage, B. Hannoyer, Scaling and internal oxidation of α-CuSn alloy, Mater. High Temp. 28 (2011) 377–382. https://doi.org/10.3184/096034011X13199009355768.

[2] F. Gesmundo, C. De Asmundis, S. Merlo, The high temperature corrosion resistance of α-phase bronzes, Mater. Corros. 30 (1979) 114–123. https://doi.org/10.1002/maco.19790300205.

[3] Y. Champion, Y. Bréchet, Effect of Grain Size Reduction and Geometrical Confinement in Fine Grained Copper: Potential Applications as a Material for Reversible Electrical Contacts, Adv. Eng. Mater. 12 (2010) 798–802. https://doi.org/10.1002/adem.200900346.

[4] L. Lu, Y. Shen, X. Chen, L. Qian, K. Lu, Ultrahigh Strength and High Electrical Conductivity in Copper, Science. 304 (2004) 422. https://doi.org/10.1126/science.1092905.

[5] Z.C. Cordero, B.E. Knight, C.A. Schuh, Six decades of the Hall–Petch effect – a survey of grain-size strengthening studies on pure metals, Int. Mater. Rev. 61 (2016) 495–512. https://doi.org/10.1080/09506608.2016.1191808.

[6] R.Z. Valiev, I.V. Alexandrov, Development of severe plastic deformation techniques for the fabrication of bulk nanostructured materials, Ann. Chim. Sci. Matér. 27 (2002) 3–14.

[7] R.Z. Valiev, R.K. Islamgaliev, I.V. Alexandrov, Bulk nanostructured materials from severe plastic deformation, Prog. Mater. Sci. 45 (2000) 103–189. https://doi.org/10.1016/S0079-6425(99)00007-9.

[8] A.P. Zhilyaev, T.G. Langdon, Using high-pressure torsion for metal processing: Fundamentals and applications, Prog. Mater. Sci. 53 (2008) 893–979. https://doi.org/10.1016/j.pmatsci.2008.03.002.

[9] S. Gourdet, F. Montheillet, A model of continuous dynamic recrystallization, Acta Mater. 51 (2003) 2685–2699. https://doi.org/10.1016/S1359-6454(03)00078-8.

[10] T. Hebesberger, H.P. Stüwe, A. Vorhauer, F. Wetscher, R. Pippan, Structure of Cu deformed by high pressure torsion, Acta Mater. 53 (2005) 393–402. https://doi.org/10.1016/j.actamat.2004.09.043.

[11] R. Pippan, S. Scheriau, A. Taylor, M. Hafok, A. Hohenwarter, A. Bachmaier, Saturation of Fragmentation During Severe Plastic Deformation, Annu. Rev. Mater. Res. 40 (2010) 319–343. https://doi.org/10.1146/annurev-matsci-070909-104445.

[12] K. Edalati, J.M. Cubero-Sesin, A. Alhamidi, I.F. Mohamed, Z. Horita, Influence of severe plastic deformation at cryogenic temperature on grain refinement and softening of pure metals: Investigation using high-pressure torsion, Mater. Sci. Eng. A. 613 (2014) 103–110. https://doi.org/10.1016/j.msea.2014.06.084.

[13] A. Bachmaier, M. Hafok, R. Pippan, Rate Independent and Rate Dependent Structural Evolution during Severe Plastic Deformation, Mater. Trans. 51 (2010) 8–13. https://doi.org/10.2320/matertrans.MB200912.

[14] C. Saldana, A.H. King, S. Chandrasekar, Thermal stability and strength of deformation microstructures in pure copper, Acta Mater. 60 (2012) 4107–4116. https://doi.org/10.1016/j.actamat.2012.04.022.

[15] B.B. Zhang, N.R. Tao, K. Lu, A high strength and high electrical conductivity bulk Cu-Ag alloy strengthened with nanotwins, Scr. Mater. 129 (2017) 39–43. https://doi.org/10.1016/j.scriptamat.2016.10.022.

[16] Y. Zhang, N.R. Tao, K. Lu, Effects of stacking fault energy, strain rate and temperature on microstructure and strength of nanostructured Cu–Al alloys subjected to plastic

deformation, Acta Mater. 59 (2011) 6048–6058. https://doi.org/10.1016/j.actamat.2011.06.013.
[17] P. Serre, R.B. Figueiredo, N. Gao, T.G. Langdon, Influence of strain rate on the characteristics of a magnesium alloy processed by high-pressure torsion, Mater. Sci. Eng. A. 528 (2011) 3601–3608. https://doi.org/10.1016/j.msea.2011.01.066.
[18] P. Zhang, J.Y. Zhang, J. Li, G. Liu, K. Wu, Y.Q. Wang, J. Sun, Microstructural evolution, mechanical properties and deformation mechanisms of nanocrystalline Cu thin films alloyed with Zr, Acta Mater. 76 (2014) 221–237. https://doi.org/10.1016/j.actamat.2014.04.041.
[19] L. Balogh, T. Ungár, Y. Zhao, Y.T. Zhu, Z. Horita, C. Xu, T.G. Langdon, Influence of stacking-fault energy on microstructural characteristics of ultrafine-grain copper and copper–zinc alloys, Acta Mater. 56 (2008) 809–820. https://doi.org/10.1016/j.actamat.2007.10.053.
[20] Y.H. Zhao, X.Z. Liao, Y.T. Zhu, Z. Horita, T.G. Langdon, Influence of stacking fault energy on nanostructure formation under high pressure torsion, Langdon Symp. Flow Form. Cryst. Mater. 410–411 (2005) 188–193. https://doi.org/10.1016/j.msea.2005.08.074.
[21] F.A. Mohamed, S.S. Dheda, On the minimum grain size obtainable by high-pressure torsion, Mater. Sci. Eng. A. 558 (2012) 59–63. https://doi.org/10.1016/j.msea.2012.07.066.
[22] K. Edalati, D. Akama, A. Nishio, S. Lee, Y. Yonenaga, J.M. Cubero-Sesin, Z. Horita, Influence of dislocation–solute atom interactions and stacking fault energy on grain size of single-phase alloys after severe plastic deformation using high-pressure torsion, Acta Mater. 69 (2014) 68–77. https://doi.org/10.1016/j.actamat.2014.01.036.
[23] E. Bruder, P. Braun, H. ur Rehman, R.K.W. Marceau, A.S. Taylor, R. Pippan, K. Durst, Influence of solute effects on the saturation grain size and rate sensitivity in Cu-X alloys, Scr. Mater. 144 (2018) 5–8. https://doi.org/10.1016/j.scriptamat.2017.09.031.
[24] X.H. An, S.D. Wu, Z.F. Zhang, R.B. Figueiredo, N. Gao, T.G. Langdon, Evolution of microstructural homogeneity in copper processed by high-pressure torsion, Scr. Mater. 63 (2010) 560–563. https://doi.org/10.1016/j.scriptamat.2010.05.030.
[25] H. Jiang, Y.T. Zhu, D.P. Butt, I.V. Alexandrov, T.C. Lowe, Microstructural evolution, microhardness and thermal stability of HPT-processed Cu, Mater. Sci. Eng. A. 290 (2000) 128–138. https://doi.org/10.1016/S0921-5093(00)00919-9.
[26] A.P. Zhilyaev, A.A. Gimazov, T.G. Langdon, Recent developments in modelling of microhardness saturation during SPD processing of metals and alloys, J. Mater. Sci. 48 (2013) 4461–4466. https://doi.org/10.1007/s10853-013-7155-6.
[27] N. Lugo, N. Llorca, J.M. Cabrera, Z. Horita, Microstructures and mechanical properties of pure copper deformed severely by equal-channel angular pressing and high pressure torsion, Mater. Sci. Eng. A. 477 (2008) 366–371. https://doi.org/10.1016/j.msea.2007.05.083.
[28] I. Lomakin, M. Castillo-Rodríguez, X. Sauvage, Microstructure, mechanical properties and aging behaviour of nanocrystalline copper–beryllium alloy, Mater. Sci. Eng. A. 744 (2019) 206–214. https://doi.org/10.1016/j.msea.2018.12.011.
[29] H.E. Kissinger, Reaction Kinetics in Differential Thermal Analysis, Anal. Chem. 29 (1957) 1702–1706. https://doi.org/10.1021/ac60131a045.
[30] L. Lutterotti, S. Matthies, H.-R. Wenk, A. Schultz, J. Richardson, Combined Texture and Structure Analysis of Deformed Limestone from Time-of-Flight Neutron Diffraction Spectra, J. Appl. Phys. 81 (1997) 594–600. https://doi.org/10.1063/1.364220.

[31] J. Xu, J. Li, C.T. Wang, D. Shan, B. Guo, T.G. Langdon, Evidence for an early softening behavior in pure copper processed by high-pressure torsion, J. Mater. Sci. 51 (2016) 1923–1930. https://doi.org/10.1007/s10853-015-9499-6.
[32] A.I. Almazrouee, K.J. Al-Fadhalah, S.N. Alhajeri, T.G. Langdon, Microstructure and microhardness of OFHC copper processed by high-pressure torsion, Mater. Sci. Eng. A. 641 (2015) 21–28. https://doi.org/10.1016/j.msea.2015.06.016.
[33] T.L. Brown, C. Saldana, T.G. Murthy, J.B. Mann, Y. Guo, L.F. Allard, A.H. King, W.D. Compton, K.P. Trumble, S. Chandrasekar, A study of the interactive effects of strain, strain rate and temperature in severe plastic deformation of copper, Acta Mater. 57 (2009) 5491–5500. https://doi.org/10.1016/j.actamat.2009.07.052.
[34] Y.S. Li, Y. Zhang, N.R. Tao, K. Lu, Effect of the Zener–Hollomon parameter on the microstructures and mechanical properties of Cu subjected to plastic deformation, Acta Mater. 57 (2009) 761–772. https://doi.org/10.1016/j.actamat.2008.10.021.
[35] Y. Zhang, N.R. Tao, K. Lu, Mechanical properties and rolling behaviors of nano-grained copper with embedded nano-twin bundles, Acta Mater. 56 (2008) 2429–2440. https://doi.org/10.1016/j.actamat.2008.01.030.
[36] W.Q. Cao, C.F. Gu, E.V. Pereloma, C.H.J. Davies, Stored energy, vacancies and thermal stability of ultra-fine grained copper, Mater. Sci. Eng. A. 492 (2008) 74–79. https://doi.org/10.1016/j.msea.2008.02.048.
[37] E. Schafler, G. Steiner, E. Korznikova, M. Kerber, M.J. Zehetbauer, Lattice defect investigation of ECAP-Cu by means of X-ray line profile analysis, calorimetry and electrical resistometry, Langdon Symp. Flow Form. Cryst. Mater. 410–411 (2005) 169–173. https://doi.org/10.1016/j.msea.2005.08.070.
[38] K. Edalati, R. Miresmaeili, Z. Horita, H. Kanayama, R. Pippan, Significance of temperature increase in processing by high-pressure torsion, Mater. Sci. Eng. A. 528 (2011) 7301–7305. https://doi.org/10.1016/j.msea.2011.06.031.
[39] S. Fürtauer, D. Li, D. Cupid, H. Flandorfer, The Cu–Sn phase diagram, Part I: New experimental results, Intermetallics. 34 (2013) 142–147. https://doi.org/10.1016/j.intermet.2012.10.004.
[40] Y. Nasedkina, X. Sauvage, E.V. Bobruk, M.Yu. Murashkin, R.Z. Valiev, N.A. Enikeev, Mechanisms of precipitation induced by large strains in the Al-Cu system, J. Alloys Compd. 710 (2017) 736–747. https://doi.org/10.1016/j.jallcom.2017.03.312.
[41] B.B. Straumal, A.R. Kilmametov, B. Baretzky, O.A. Kogtenkova, P.B. Straumal, L. Lityńska-Dobrzyńska, R. Chulist, A. Korneva, P. Zięba, High pressure torsion of Cu–Ag and Cu–Sn alloys: limits for solubility and dissolution, Acta Mater. (2020). https://doi.org/10.1016/j.actamat.2020.05.055.
[42] E. Schafler, G. Steiner, E. Korznikova, M. Kerber, M.J. Zehetbauer, Lattice defect investigation of ECAP-Cu by means of X-ray line profile analysis, calorimetry and electrical resistometry, Langdon Symp. Flow Form. Cryst. Mater. 410–411 (2005) 169–173. https://doi.org/10.1016/j.msea.2005.08.070.
[43] J. Gubicza, S.V. Dobatkin, E. Khosravi, Reduction of vacancy concentration during storage of severely deformed Cu, Mater. Sci. Eng. A. 527 (2010) 6102–6104. https://doi.org/10.1016/j.msea.2010.05.088.
[44] L.H. Su, C. Lu, L.Z. He, L.C. Zhang, P. Guagliardo, A.K. Tieu, S.N. Samarin, J.F. Williams, H.J. Li, Study of vacancy-type defects by positron annihilation in ultrafine-grained aluminum severely deformed at room and cryogenic temperatures, Acta Mater. 60 (2012) 4218–4228. https://doi.org/10.1016/j.actamat.2012.04.003.
[45] J.D. McGervey, W. Triftshäuser, Vacancy-formation energies in copper and silver from positron annihilation, Phys. Lett. A. 44 (1973) 53–54. https://doi.org/10.1016/0375-9601(73)90957-2.

[46] D.A. Porter, K.E. Easterling, Phase Transformations in Metals and Alloys, Van Nostrand Reinhold, 1981.
[47] J. Freudenberger, A. Kauffmann, H. Klauß, T. Marr, K. Nenkov, V. Subramanya Sarma, L. Schultz, Studies on recrystallization of single-phase copper alloys by resistance measurements, Acta Mater. 58 (2010) 2324–2329. https://doi.org/10.1016/j.actamat.2009.12.018.
[48] M.B. Bever, D.L. Holt, A.L. Titchener, The stored energy of cold work, Prog. Mater. Sci. 17 (1973) 5–177. https://doi.org/10.1016/0079-6425(73)90001-7.
[49] W.D. Callister Jr, Materials Science and Engineering - An Introduction (5th ed.), Anti-Corros. Methods Mater. 47 (2000). https://doi.org/10.1108/acmm.2000.12847aae.001.
[50] T. Ungár, I. Dragomir, Á. Révész, A. Borbély, The contrast factors of dislocations in cubic crystals: the dislocation model of strain anisotropy in practice, J. Appl. Crystallogr. 32 (1999) 992–1002. https://doi.org/10.1107/S0021889899009334.
[51] R.Z. Valiev, E.V. Kozlov, Yu.F. Ivanov, J. Lian, A.A. Nazarov, B. Baudelet, Deformation behaviour of ultra-fine-grained copper, Acta Metall. Mater. 42 (1994) 2467–2475. https://doi.org/10.1016/0956-7151(94)90326-3.
[52] S.X. Ding, C.P. Chang, P.W. Kao, Effects of Processing Parameters on the Grain Refinement of Magnesium Alloy by Equal-Channel Angular Extrusion, Metall. Mater. Trans. A. 40 (2009) 415. https://doi.org/10.1007/s11661-008-9747-3.
[53] U.F. Kocks, H. Mecking, Physics and phenomenology of strain hardening: the FCC case, Prog. Mater. Sci. 48 (2003) 171–273. https://doi.org/10.1016/S0079-6425(02)00003-8.
[54] O. Renk, R. Pippan, Transition from thermally assisted to mechanically driven boundary migration and related apparent activation energies, Scr. Mater. 154 (2018) 212–215. https://doi.org/10.1016/j.scriptamat.2018.05.052.
[55] O. Renk, P. Ghosh, R. Pippan, Generation of extreme grain aspect ratios in severely deformed tantalum at elevated temperatures, Scr. Mater. 137 (2017) 60–63. https://doi.org/10.1016/j.scriptamat.2017.04.024.